INTERNATIONAL ATOMIC ENERGY AGENCY
UNITED NATIONS EDUCATIONAL, SCIENTIFIC AND CULTURAL ORGANIZATION

INTERNATIONAL CENTRE FOR THEORETICAL PHYSICS
34100 TRIESTE (ITALY) - P.O.B. 586 - MIRAMARE - STRADA COSTIERA 11 - TELEPHONE: 2240-1
CABLE: CENTRATOM - TELEX 460392 - I

SMR/291 - 21

SPRING COLLEGE IN CONDENSED MATTER
ON
"THE INTERACTION OF ATOMS & MOLECULES WITH SOLID SURFACES"
(25 April - 17 June 1988)

IMAGING OF STRAINED STATE IN METALS BY ION BOMBARDMENT METHOD

Lev. B. SHELYAKIN
Faculty of Physics
Moscow State University
117234 Moscow
U.S.S.R.

Imaging of strained state in metals by ion bombardment method

Ion bombardment is known to be used extensively in visualizing the surface structure of various materials (see for example, V.E. Yurasova, B.V. Spivak, and A.O. Krokhina. In: Present-Day Electron Microscopy, A.S. Popov Sci. Techn. Amalgamation for Radioelectronics, Moscow, 1965, pp. 54-89). This is explained by the fact that the atoms binding energy of the located at grain boundaries and near various defects differs from that of the atoms located on crystal faces. In case of composite materials, the individual phases and regions enriched by one of the constituent elements of a given material are visualized. It is of interest to find out whether irradiation by ions can visualize the deformed zones.

In their works, Askerov and Nasrullaev have shown that the sputtering yield S of a material varies under the effect of a mechanical load resulting in plastic deformation and, particularly, in a decrease of grain size.

Since the grain size decrease under plastic deformation gives rise to a great number of weakly-bound atoms (located at crystal edges and vertices), any change in grain size must have a particularly strong effect on the sputtering yield S in the range of low ion energies.

Figs 1 ~~and 2~~ shows the sputtering yield S (in relative

units) versus Hg^+ ion energy for the Cu and Ag samples under compression at different pressures. As the ion energy increases, the dependence S f(E) rises linearly.

The role of plastic deformation, that is, the role of grain size decrease, is clearly seen in Figs 3 ~~and 4~~ which shows the dependence of the sputtering yield S for Cu and Ag on the compression of the sample. The sputtering yield increases very rapidly with pressure. Accordingly, the threshold sputtering energy changes as a function of plastic deformation, as seen in Fig. 5. We see that, as the pressure rises, the threshold energy decreases rapidly and reaches low values of ~ 12 eV. Obviously, the processes occurring in crystal depth play an ever increasing role with rising the incident ion energy. This fact is reflected in the dependence of the ratio $S_{deform}/S_{undeform}$ on ion energy (see Fig. 6). We see that the ratio $S_{deform}/S_{undeform}$ falls rapidly with increasing the incident ion energy in the low-energy range and approaches a certain constant.

This dependence seems to me to be indicative of a very important circumstance. Namely, if an examined sample has a strongly deformed area, the highest contrast between the deformed area and the undeformed zone arising from sputtering the two regions can be attained at the lowest possible incident ion energies close to the sputtering threshold. Nasrullaev and Askerov have demonstrated the potentialities of this method when studying archeological samples.

As the bombarding-particle energy increases, however, other processes will show themselves also, namely, the selective sputtering, the radiation-stimulated diffusion of defects and impurities, the ion embedding, the ion mixing, and the creation of stresses under ion embedding. These processes may affect the creation of a contrast between the initially-deformed and undeformed zones.

The present work examines the feasibility of visualizing the strained zones in metals by ion bombardment method at high energies of incident particles (Ar^+ ions of energies of up to 40 keV, 0.8 MeV electrons, 37 MeV protons).

Experimental techniques

Targets of different materials were prepared in order to study the feasibility of visualizing the strained zones in metals. Local strains were created mechanically on the targets. The upper visible deformed layer having been removed, the targets were subjected to irradiation, thereby giving rise to a contrast between deformed and undeformed (or little deformed) zones. For the sake of comparison, the deformed areas were also visualized by electrochemical etching and by thermic heating in vacuo.

The targets to be studied were cylinders of 30 mm diameter and 10 mm height. They were prepared of the materials whose main characteristics are presented in Table 1. Bronze ($Cu_{0.87}Sn_{0.13}$) was chosen as an alternative new material. In this alloy, the diffusion effects in the plastic deformation zone are clearly expressed because of very different atomic radii (d_{Cu} = 0.128 nm, d_{Sn} = 0.158 nm).

A strained zone was created on one of the bases of a sample using a standard digital mark of 2 under hydraulic pressure. It should be noted that in case of a faint contrast of a deformed

Table 1

Material	Hardness $H_B \cdot 10^7$ /m^2	Content C, %	Heat treatment
Copper	27	-	-
Duraluminum	70	-	Hardened
Steel-3	131	0.14 - 0.22	-
Steel-20	163	0.17 - 0.24	-
Steel-45	229	0.42 - 0.49	-
Steel-40X	370	0.37 - 0.45	Hardened
Steel-V8	350	0.69 - 0.73	-

Table 2

Material	Ordinary number of deformed zone				
	1	2	3	4	5
Copper	300	500	750	1000	-
Duraluminum	300	500	750	1000	1250
Steel-3	600	850	1000	1300	1500
Steel-20	500	800	1000	1380	1500
Steel-45	500	800	1050	1250	1500
Steel-40X	500	800	1000	1500	-
Steel-V8	550	800	1000	1500	2000

zone with certain mark (digit 2 in the given case), the man's eye "completes" the missing elements of the observed pattern, just as in aeroarcheology. In such a way, the entire deformed zone gets visualized clearly and any possible error due to a random contrast fluctuation is excluded. The range of loads for each sample was chosen depending on the hardness of a given material. The loads are given in Table 2 in kg.

After a deformed zone was created mechanically (by successive grinding and polishing), the metal surface layer was removed until digit 2 disappeared completely, whereupon the sample was ion-irradiated. The irradiation gave rise to a deformed-zone contrast, so digit 2 became visible again. The operation was repeated until the deformed-zone contrast disappeared completely. Simultaneously, the sample structure was examined at various depths H measured from the surface layer of the sample where the digit 2 trace stopped being visible after mechanical polishing. Besides, the width of the digit was measured as a function of H at a certain place and the maximum depth H_{max} where the contrast disappeared was found. The dependence of the mean grain size δ in a deformed zone on H was also studied. The mean grain size was obtained by dividing the area of a given zone of surface microphotograph by number of grains in the zone.

The deformed-zone contrast was observed visually and with a binocular microscope. The metallographic and scanning electron microscopes were used to measure the trace width D and to study the structure. The depth of a removed surface layer was inferred from micrometer readings after each etching step.

The samples were irradiated by Ar^+ ions at 4 keV (in subnormal discharge at a 1.5-2.0 mA/cm^2 current density) and 40 keV (in magnetic mass-separator at a 0.4 mA/cm^2 current density). The irradiation periods lasted until a deformed-zone contrast appeared, namely, for 15 min in case of copper under 4 keV ion bombardment and for 2-2.5 hours in case of steels under 40 keV ion bombardment.

Apart from Ar^+ ion irradiation, the samples were irradiated by 0.8 MeV electrons and 37 MeV protons of a 2×10^{17} particle/cm^2 dose at current densities j_e = 10-15 mcA/cm^2 and j_p 16 mcA/cm^2.

The temperature of the samples was 150°-200° in case of 4 keV Ar^+ ion bombardment, was 30° in case of 40 keV Ar^+ ion bombardment, and did not exceed 100° in case of irradiation by electrons and protons.

The effect of copper sample temperature within a 300°-700° interval on the strained-state zone contrast was also studied. The samples were heated by contact in vacuo, the temperature was measured within a thermocouple. The heating time was 30-40 min.

The feasibility of visualizing strained-state zones was studied by electrochemical etching of copper and steel-20 samples. In the steel-20 experiment, a 3% Fe_2SO_4 solution was used as electrolyte, a stainless steel plate was the second electrode, the voltage between the electrodes was 80 V, the current density on a sample was 71 mA/cm^2, and the etching time was 7 min. In the copper experiment, orthophosphoric acid was used as electrolyte, a lead plate was the second electrode, the voltage between the electrodes was 8 V, the current density on a sample was 14.3 mA/cm^2, and the etching time was 20 min.

Results and discussion

Visualization of a deformed zone under ion bombardment

Ion bombardment was used to examine the microstructure, size, shape, and contrast of a deformed zone at different depths in samples, depending on target material and on incident ion energy. As mentioned above, all measurements were taken after using mechanical polishing to completely remove the image of the digit 2 mark applied at definite loads. The digit appeared to be visible again on the sample surface after ion etching even when a substantial surface layer was removed by polishing. The depth h_{max} of the removed layer was defined by the target material properties, by the load used to apply the mark, and by the ion bombardment conditions. The maximum depth at which the digit was still discernable reached sometimes 1.0-1.5 mm. The digit 2 trace was observable because of the ion bombardment-made contrast between deformed and undeformed (or little deformed) zones.

Changes of the sample microstructure at various depths of a deformed zone

Such changes were traced for the steels indicated in Table 1. In all cases, the mean grain size increased rapidly until reaching a certain depth h, whereupon the grain size approached, at a much slower rate, the value characteristic of undeformed zones (see Fig. 6). In case of harder materials (steels 40X and V8), the first stage is steeper and the transition to a lower rate of increasing δ is more clearly expressed than in case of milder

materials (steels 20 and 3).

The shape of the $\delta(h)$ curves in Fig. 6 can be explained as follows. The creation of a deformed zone (the application of the digit mark) is accompanied by pressing-out of the sample material by the stamp, that is, takes place in the yield region of the material. The upper layers of a deformed zone (small h values) are characterized by a strong deformation corresponding to the yield of a given material and by substantial changes of grain size. At the extreme points of the curves the grain size increase rate gets very low and the grain size reaches 70-90% of that in undeformed zone. The closest approach to the undeformed=zone grain size is observed for harder materials and at smaller loads. The dependences $\delta(h)$ seem to reflect two regions of a deformed zone. The first region corresponds to the yield region of materials and the second (deeper) region corresponds to the region of residual plastic strain. In the deeper layer, underlying the layer h with changed grain size, the target zone of elastic deformation must be located.

Depth of a deformed zone

At a given load, such depth is defined by mechanical properties of a given material, namely, by its hardness and plasticity with inverse dependence between them (hardness rises with decreasing plasticity and vice versa) |. In case of steels, hardness and plasticity are defined, to a great extent, by carbon content and by heat treatment.

In maximum depth h where the deformed-zone trace is visualized, depending on material hardness H_B, was obtained for steels at the load $P = 1500$ kg (Fig. 7).

An optimal combination of hardness and plasticity seems to be necessary for obtaining the highest value of h_{max}. In case of nonhardened steels (steels 3, 20, 45), the rise of hardness ensures that deformation will be transferred the deeper depths. In case of hardened steels (steels 40X, V8), their too high hardness prevents deformation from occurring at deep depths.

Fig.8 presents the h_{max} variations as a function load P on the stamp for various materials. In the descending order of h_{max}, the examined materials form the following sequence: steel 45, steel 20, duraluminum, steel 3, copper, steel 40X, and steel V8. The nonlinear behaviour of $H_{max}(P)$ is probably explained by the fact that a deformed zone is created (the digit mark is applied) in the yield region of materials where the deformation is a linear function of loads .

The width of deformed zone at different depths in samples

Observing the digit 2 image has shown that, as the upper layers of a sample are removed, the image contrast and the digit size are changed. Henceforth, the digit line width will be called the deformed-zone width.

Fig.~~9~~ shows the consecutive images of the digit 2 trace after several operations of polishing and etching. It is seen that the clear boundary of the trace disappears rather rapidly, just in correpondence with the removal of a layer whose depth, in turn, corresponds to the linear behaviour of the dependence of the mean grain size on depth (Fig. ~~6~~, the beginning of the curve). It should be noted that the overall view of the mark was still observable

after removing a layer of substantial depth, although the grain sizes in the deformed and undeformed zones were already the same.

The visible contrast of the digit image was used to infer the deformed-zone width D at different depths. At small depths (h 0.05-0.2 mm), the boundary between deformed and undeformed zones was clearly seen (it was darker in the pictures). The depths at which the boundary was observable are different for different materials and decreases with increasing hardness. In the hardened steels, the boundary disappeared in practice immediately.

At the medium and deep depths (h 0.1-0.3 mm), the deformed zones differ from the undeformed zones in their colour. In all the materials (except duraluminum) the deformed zones were of lighter colour compared with the undeformed zones. The general trend of the dependence D(h) is shown in Fig. ~~10~~ 9. As h increased, the deformed-zone width D also increased. In case of hard materials (steels 45, 40X, and V8), the deformed zone width reached its visible maximum rapidly and then decreased slowly with further increasing h (the plateau in Fig. ~~10~~ 9). Only before the ultimate disappearance of the deformed-zone contrast, did the width D decreased rapidly. In case of milder materials (copper, duraluminum, steels 3 and 20), the width D increased gradually with rising h and, after that, decreased somewhat more rapidly. In some cases the width D increased again at deep depths. [fig 10]

The comparison among the results displayed in Figs ~~9~~ and ~~10~~ 9 has shown that the h region with a rapid growth of the mean grain size, that is, the yield regions of materials, is in correspondence with the region of rapid rise of D(h). However, the dependence D(h) appears to be more gradual compared with the dependence of the mean grain size (for example, in case of steel 20). In all the curves shown in Fig. 7 the observed bend corresponds to the depth h at which the visible boundary between the deformed and undeformed zones disappeared. The largest gradient of strains and, hence, the greatest number of discontinuities, shears, etc. occur at the deformed-zone boundary because of the deformation inhomogeneity. At high strains (in the yield region of materials), therefore, the deformed-zone boundary is highly inhomogeneous and must get expressed more clearly under ion bombardment in virtue of a higher sputtering ability.

From the comparison between Figs 8 and 10 (for example, in case of steel 20) it is seen that the observed deformed-zone contrast was preserved for a longer period compared with the period during which the difference between the deformed and undeformed zone grain sizes disappeared. The image contrast was suggested to be due to not only the difference in the initial (before etching) structures of the deformed and undeformed zones, but also the radiation-stimulated diffusion of defects and impurities arising in the course of irradiation in the field of mechanical strains. This effect must be expressed more clearly in the materials where the amount of impurities and defects is sufficient for the deformed-zone contrast to be increased by their diffusion, but is still insufficient to prevent them from moving in the mechanical strain field to the distances where the deformed-zone contrast can occur. In our case, the copper sample satisfies these requirements.

Size of visualized deformed zone at different energies of sputtering particles

The size of visualized deformed zone was characterized by two parameters, namely, by the maximum depth h_{max} of visualization and by the visible trace width D. The two parameters were compared at the bombarding Ar^+ ion energies of 4 and 40 keV for copper and steel 20. These materials differ in homogeneities and in impurity contents and, at the same time, are succeptible to plastic deformation, thereby facilitating observation of a strained region.

The effect of the bombarding Ar^+ ion energy on the maximum visualization depth of a deformed zone

Our studies have shown that the rise of the bombarding Ar^+ ion energy from 4 to 40 keV leads to increasing the maximum visualization depth h_{max} of the deformed zones in copper and steel 20 (~~see Fig. 11~~). In case of steel 20, h_{max} varied from 40% at P = 600 kg to 10% at P = 100 kg. In case of copper, h_{max} increased by a factor of 5 throughout the range of P from 340 to 750 kg.

The increase in the maximum visualization depth h_{max} of a strained region with the bombarding ion energy may be due to the radiation-stimulated diffusion of defects and impurities. As the energy E of incident ions increases, the number of the irradiation-produced defects also increases. The defects migrate when affected by local strains and are absorbed by sinks, namely, by dislocations, pores, grain boundaries, etc. Accordingly, the impurity diffusion is facilitated. By itself, the diffusion of defects and impurities can change the deformed-zone contrast and result in a change of sputtering yield which, in turn, enhances the contrast and makes it sufficient for being observed at deep depths. A stronger dependence $h_{max}(E)$ in case of copper, compared with steel 20, may be explained by more favourite (compared with the case of steels) conditions of the diffusion of impurities and defects to great distances, as mentioned above.

The effect of the bombarding Ar^+ ion energy on the visible deformed-zone width

As in case of measuring the h_{max} value, an increase in the incident ion energy resulted in an increased visible deformed-zone width D for copper and steel 20. In case of steel 20, the increase in D and in h_{max} was insignificant and the D(h) form did not vary. In case of copper, the dependence D(h) was of a complicated form (Fig.12). At the depth near h_1, where the difference in the grain size between deformed and undeformed zones disappeared, the dependence D(h) when the incident Ar^+ ion energy increased up to 40 keV was similar to the dependence at E = 4 keV. Whereas, however, the deformed-zone contrast near h_1 disappeared at E = 4, it was presented with increasing h at E = 40 keV and the visible deformed-zone width increased sharply.

Fig. 13 shows a series of the dependences D(h) for copper obtained at different loads P for 40 keV incident Ar^+ ions. As the load P increases, the minimum of the curves goes downwards and shifts towards higher values of h.

The shape of the D(h) curves for copper under 40 keV Ar^+ ion bombardment may be explained using the scheme presented in Fig. 14. The double shading shows region 1 corresponding to yield and plastic deformation. Regions 2 and 3 correspond to elastic deformation. The defects and impurities located in region 3, but close to regions 1 and 2, will diffuse, first of all, towards region 1 because of the largest gradient of mechanical strains observed in this direction. This circumstance can account for the narrowing of the deformed zone. As the load P rises, the deformation region shifts to deeper layer of a sample. So, as P rises, the boundary of a much defected layer shifts to higher values of h, in correspondence to the shift of the curve minimum in Fig. 13 also to higher values of h. The narrowing of the visualized deformed zone near h_1 from 0.45 mm at P = 310 kg to 0.28 mm at P = 750 kg seems to be due to the fact that the lower boundary of the plastic-deformed layer descends to a deep depth (from 0.25 to 0.5 mm) where the target material is obviously more difficult to undergo plastic deformation.

Visualization of a deformed zone under irradiation by high-energy particles (0.8 MeV electrons and 37 MeV protons)

Strained state of materials under high-energy electron and proton irradiation was visualized with a view to elucidating the role of the radiation-stimulated diffusion in creating a deformed-zone contrast. Samples of stainless steel 1 x 18H9T with the digit 2 layer removed completely were irradiated by 0.8 MeV electrons of a 2 x 10^{17} particle/cm^2 dose and by 37 MeV protons of the same dose.

The electron irradiation gave rise to a very faint contrast between deformed and undeformed zones (which was much weaker than in case of ion bombardment). A Varian Auger-spectrometer at a 10^{-10} mm Hg was used to analyze the composition of sample surface after electron irradiation. A continuous carbon layer was observed on the surface without ion purification. After the purification by 2.5 keV Ar^+ ions, the Auger analysis revealed an increased carbon content in deformed zone (compared with underformed zone) at depths of about 50, 250, and 500 Å.

The 0.8 MeV electrons penetrate through the entire depth of the sample ($\sim$8 mm). They cannot give rise to a sputtering process because at such energies the energy loss, with the momentum turned to the irradiated surface, proves to be too high, so the energy transferred to the surface atoms is to be insufficient to induce their sputtering. However, when moving through the sample, the 0.8 MeV electrons produce various defects. The threshold electron energy for producing the Frenkel pairs is $E_{thr} = (M/m_e)E_d$, where M is atomic mass, $E_d = 25$ eV is energy to displace an atom from a lattice site; m_e is electron mass, $M/m_e \sim 10^5$, that is, $E_{thr} \sim 0.6$ MeV. Therefore, the 0.8 MeV electrons produce a very small number of the Frenkel pairs in iron and copper, but are capable of displacing the atoms of light impurities (for example, carbon) from lattice sites to interstitials where they are more movable and can diffuse. The diffusion flux gets directed in the presence of a strain gradient, thereby giving rise to an excess or a deficit of impurities in the maximum deformation zone. Motions of atoms in interstitials were observed by M. Kiritan et al. (1975) in some metals

under electron irradiation at, however, higher electron energies (1-2 MeV). Probably, carbon forms complexes with vacancies in the same manner as helium and deuterium. This problem was studied by M.I. Baskes and W.D. Wilson in 1976 and by V.D. Alimov, A.E. Gorodetsky, and A.P. Zakharov in 1984. Such complexes are notable for their high mobility which enhances the diffusion of impurities.

In the absence of electron irradiation, the carbon diffusion in the mechanical strain field would be insignificant. To verify this, the XPS-spectrum of carbon was obtained for an identical sample not irradiated by electrons. The XPS-analysis was chosen because it makes it possible to obtain a signal to which a much greater target layer contributes, compared with the Auger analysis. No increase was observed in the carbon content on undeformed zone not irradiated by electrons.

The proton irradiation. In the specimen irradiated by the 37 MeV protons penetrating, like electrons, through the entire sample depth, the deformed-zone contrast increased sharply compared with the electron irradiation and got sufficient for being observed visually.

The sputtering process is very insignificant under bombardment by protons of the like energies. However, the number of the produced defects is substantially (by several orders) higher compared with the 0.8 MeV electron irradiation. Therefore, the enhanced image contrast under the proton bombardment must be attributed, first of all, to the strong radiation-stimulated processes of the diffusion of defects and impurities.

Visualization of a deformed zone by heating in vacuo

Since the samples were heated under ion bombardment, it was of interest to study the sample temperature effect on the contrast of deformed zone image. With this purpose, a copper sample prepared in the conventional way with a digit 2 trace was heated in vacuo at 300-700° without any preliminary irradiation. At temperatures above 300°, a deformed-zone contrast occurred, but it was much weaker than in case of ion bombardment. When visualizing the deformed-zone contrast, the value of h_{max} was smaller than in case of ion bombardment. A contrast between deformed and undeformed zones arose probably from thermodiffusion of defects and impurities. The copper sample did not show any noticeable evaporation at the above mentioned temperatures.

Visualization of a deformed zone by electrochemical etching

The electrochemical etching carried out for the sake of comparison has shown that a deformed-zone contrast gets visualized only at the depths where the difference in the grain sizes between deformed and undeformed zones is still substantial. Table 3 presents the relative data bearing on the visualization of deformed zone by electrochemical and ion etchings.

The data of Table 3 demonstrate the advantages of ion irradiation when visualizing strained zones in metals. It should be noted that a strained-state zone visualized by ion irradiation is preserved for a long time, whereas in case of electronchemical etching a deformed-zone image disappears in open air at a such high rate that the necessary microscopic examination and photographing cannot be carried out in most instances.

Table 3

The maximum visualization depths of deformed zones for electrochemical and ion etchings

Material	Load, P kg	Electrochem. etching, mm	Ion irradiation, mm	
			E = 4 keV	E = 40 keV
Copper	500	0.17	0.21	0.89
Steel 3	1000	0.35	0.68	0.74

The role of the diffusion process in, and its contribution to, the development of deformed-zone contrast

A number of studies in last few years have shown the ability of ion bombardment to make visible the areas of high plastic deformation in various materials exposed to the bombardment by ion beams of threshold or keV energies. It was suggested that the preferential sputtering and atom segregation of deformed surface layers are responsible for the formation of the contrast for this visualization.

The aim of the present research was to establish the role and the contribution of both contaminant and implanted atom diffusion in the formation of the pattern contrast.

Experimental techniques

Copper and steel (ST 20) samples were used as target materials since they (a) differ significantly in properties, (b) are easily deformed and processed, (c) have already been studied and some results on imaging of the surface areas under strain were available for comparison . Bronze $(Cu_{0.87}Sn_{0.13})$ samples were chosen as an alternative new material for which no data on such imaging were known. In this alloy the diffusion effects in the plastic deformation zone are expected to be substantial due to the quite different atomic radii (0.128 nm for Cu and 0.158 nm for Sn atoms) .

Fig. 15 shows the shapes of the samples and the places where loads were applied, as well as the areas whence information was

readout. The deformed surface zones were created by using a standard digital mark of 1. The mark was formed under different loads which ranged from 350 to 1000 kg, depending on the hardness of a given material. The marks were applied on only cubic samples. The horseshoe-shaped samples were compressed until plastic deformation occurred. Following the marking, the sample thickness was measured in the vicinity of the mark, whereupon the depth of a groove made by marking was found. Then the upper layers of each sample were removed, in some cases until the mark disappeared completely.

The final stage was to polish the surface with an optical polishing paste and to subject the sample to ion etching using the ILU-2 and VUP-2K mass separators or the Ardenne ion source. The Ar^+ energy was varied from 4 keV to 40 keV, the current density was 0.35-0.56 mcA/cm^2, the etching time was 0.5-3 hours. The Ne^+ energy was 20 keV, the current density was 0.8 mcA/cm^2, the irradiation time was 0.3-3 hours.

The samples with the applied digit mark were irradiated from above, on the plane where the strain occurred, and from its lateral side, on the plane perpendicular to the mark. The horseshoe-shaped samples were irradiated in the zone of the strongest strain (the shaded area in Fig. 15).

The study of the structure of irradiated surface regions and the X-ray microanalysis were both carried out in a combined XEM/XMA (Camebax) machine which allowed us to follow the profile distribution of various elements in the deformation zone. The distributions were measured by using either electron probe scanning within a short distance span (up to 250 um) or automatic table shift over 3000 μm for a static probe. In the microanalysis chamber the sample was oriented in such a way that the possible roughnesses in the deformation zone were aligned perpendicular to the electron probe scanning line and to the plane through the sample and the spectrometers. The profile distributions were measured by using small angle exit to the spectrometer in order to minimize the sensitivity to the surface roughness. Such precautions enables us to avoid the errors related to the surface roughness which can be due, for instance, to preferential sputtering effects . The microanalysis of the copper and steel samples was carried out simultaneously at two levels, K_α C (447 nm) and K_α Ar (419 nm). The X-ray emission was detected by using crystals of ODRb for the carbon and PET for the argon lines. For the analysis of bronze alloy samples the K Cu (15.4 nm) and L_α Sn (36 nm) lines were used, detectors being LiF and PET crystals respectively. The accelerating voltage for the analysis was 15 kV and the probe current was 10^{-7} A. The exit angle of the X-ray radiation in the machine used was 45°.

The quantitative analysis of the impurity concentration and its change in the diffusion zone was performed using standard techniques incorporated in a 'ZAF' computer programme distributed by 'Tracor'. The computer code is based on the assumption that the relationship $C = K \cdot k_Z \cdot k_A \cdot k_F$ is valid, where C is the concentration of the analysed element, K is the ratio of the X-ray intensities measured in the microanalysis and corrected for the dead time and the background, k_Z is the correction due to the atomic number, k_A is the adsorption correction, k_F is the correction factor for the fluorescence due to the characteristic X-ray emission.

Experimental results

In order to elucidate the reasons for formation of the contrast in the case where grain sizes of deformed and undeformed surface regions do not differ significantly, experiments on irradiation of steel samples by 40 keV Ar^+ ions were carried out. The digit mark was made by using a load of 1000 kg. In these conditions the depth of the mark groove was evaluated to be 0.36 mm which amounted to 2/3 of the maximum depth where the deformation of the material can still be observed. It should be pointed out that in this case carbon was the only impurity element which could easily diffuse in the strain fields as a result of quite different atomic radii for carbon ($d_C = 0.077$ nm) and other substrate element ($d_{Fe} = 0.126$ nm) .

Results of the X-ray structure analysis of deformed surface regions are presented in Figure $1\overset{5}{6}$. Enhanced intensities of the X-ray peaks corresponding to carbon were found in the deformed zones and on their boundaries with the undeformed parts of the surface.

The distribution of carbon and argon in the deformation zones was studied also on copper samples. In this case the wafer was marked with a digit by using a load of 540 kg. The cross=section of the sample was irradiated by 40 keV argon ions in the ILU-2 mass separator.

Argon is known to move quite easily in the deformed region . This is mainly due to the fact that it is not chemically active and therefore no chemical compounds are formed.

In Fig. 17 we have illustrated the carbon and argon distributions along the line shown in Fig. 17(b). The spectra indicate that the most heavily deformed region (numbered 1 in Fig. 17(b)) is depleted of argon. On the contrary, in the regions of small elastic deformation and outside the deformation zone a considerable amount of argon was found. The carbon spectra (Fig. 18) of heavily deformed areas indicate that the flow deformation zone of the material is also enriched with carbon.

Fig. 19 shows the carbon distribution spectra of a copper sample following a polishing out of the upper layers of thickness 0.31 mm and thermal annealing in vacuum at 650°C for 1 h. The distribution profile of the carbon line indicates enhanced content of this element in the boundary between the deformed and undeformed material.

The carbon and argon impurities amounted to only a fraction of 1% and, therefore, their redistribution in the deformation zone was difficult to follow. Bronze, containing 87% Cu and 13% Sn, seemed to be a more convenient alloy for studying the impurity redistribution resulting from the radiation-enhanced diffusion in the deformation zone.

The bronze samples were marked by using loads of 350 kg and 700 kg. The enhanced diffusion of the tin in the strain field was studied on these samples after the top layers of 0.25 nm were removed (the reference level being the bottom of the groove). Diffusion of the tin from the flow deformation zone was clearly observed. The extension of the diffusion area at this depth was as large as 200 µm (Fig. 20). The tin content in the zone of plastic deformation was 2-3% higher than in the original material. As seen in Fig. 20, the behaviour of copper distributions in the flow and plastic deformation zones is just the opposite

to that of the tin distribution.

The irradiation of bronze samples by 40 keV Ar^+ ions in the ILU-2 mass separator for 30 min resulted in the visual appearance of the digital mark on the target surface. The contour of the mark was protruding above the base sample surface by up to 0.5 µm. During the irradiation the ion stimulated segregation occurred as a result of preferential sputtering of tin and the enrichment of the surface with copper atoms (Fig. 21). In the tin-diffusion zones the concentration of this element after the irradiation was reduced to values corresponding to the undeformed surface of the sample (Fig. 22) due to a more intensive sputtering of tin.

To elucidate the role of the strain sign, we irradiated the horseshoe-shaped samples of the above discussed materials with 20 keV Ar^+ and Ne^+ ions. The horseshoe side surface was analyzed at the point of the maximum curvature (Fig. 15) before and after the deformation occurrence and with and without irradiation in both cases. From Fig. 23 it is seen that the Ar content proved to be increased in the compression zone and to be decreased in the tensile strain zone compared with nondeformed region (near the median line of the sample). Deviations from this pattern were observed at the edges of the sample.

The behaviour of the Ar and Ne ion distributions in the horseshoe-shaped samples is the same. The implanted-ion and carbon distribution profiles are presented in Figs 23 and 14.

All the distributions were readout at small and medium irradiation doses. An increase of irradiation time up to 90 min results in a levelling of the Ar and Ne distribution profiles, so their concentrations in the compression zone and outside the deformation zone get equal.

Discussion

We studied the impurity distribution on the deformed parts of the metal surface exposed to ion irradiation. In the copper and steel substrates, easily diffusing impurities are carbon and argon and their redistribution was followed.

The enhancement of the carbon contents in the deformed regions of the copper and steel samples (Figs 16-18) in comparison to that of undeformed areas can be associated with the highest strain gradient on the boundary between deformed and undeformed areas after the mechanical treatment. As a result of shifts and discontinuities in the boundary region the highest inhomogeneity appears. Due to the considerable size reduction of the microstructure there appear additional defect traps such as grain boundaries. They make the diffusion of the impurity atoms in the deformed regions easier. Meanwhile, the radiation enhanced diffusion itself contributes to the modification of impurity concentration in the deformed regions.

Analysis of the copper sample cross-sections indicated that the most deformed surface regions (i.e. flow and plastic deformation zones) are depleted of argon but enriched with carbon. On the contrary, the elastic deformation zone and undeformed parts the sample surface are enriched with argon and depleted of carbon. In this case the carbon behaves as in other deformed materials, i.e. diffuses into the mechanical strain zones.

Since the argon is able to move easily along the defects, it can either go deep in the bulk or to be released back into the vacuum, in both cases leaving depleted surface layers.

The most deformed top layers of the samples were enriched

with carbon. This behaviour of carbon atoms again makes clear its role in the formation of the visual contrast of the deformed surfaces.

In the thermal imaging of the strain zones of copper samples the main role in the formation of the contrast between deformed and undeformed regions can be attributed to the thermal diffusion of defects in the zones of highest deformation (Fig. 19).

The most prominent effect of the diffusion processes was found in the bronze samples. Since the tin concentration was much higher in comparison to that of carbon and argon, even small changes in this concentration could be detected easily. Figs and show schematically how the surface topography and the corresponding tin and copper concentrations in the diffusion zones changed after polishing and ion beam irradiation of the samples.

The imaging of the deformation zone in the case of bronze samples could be due to the difference in the sputtering coefficients. Indeed, the tin sputtering coefficient is higher than that of copper targets so that the modified surface concentrations of these atoms in the deformed regions result in a smaller sputtering rate in comparison to the rest of the surface. As a consequence, after the irradiation the deformed areas seemed to protrude above the other surface parts.

The increased irradiation doses (up to $\sim 10^{19}$ ion/cm^2) was noted to result in the identical contents of the implanted noble gas in the deformed and undeformed zones. The decreased doses (to $\sim 10^{18}$ ion/cm^2) resulted in different implanted noble gas contents in the zones. This effect is probably due to high compressive strains in case of high doses resulting in a levelling of the strain values and sign in the surface layer.

In conclusion, the radiation enhanced diffusion of the contaminant and implanted impurity atoms contributes to the formation of the contrast of the deformed surface regions by changing the surface topography due to modified sputtering rates of the deformed and undeformed areas and different atomic concentrations at the surface.

Figs 1 and 2. Sputtering yield S (in relative units) versus Hg^+ ion energy for Cu and Ag specimens under compression at different pressures.

Figs 3 and 4. Sputtering yield S for Cu and Ag as a function of the compression of the sample. Ion energy are $E = 30$ and 40 eV.

Fig. 5. Variations of threshold sputtering energy as a function of plastic deformation.

Table 1. In the table, the materials are presented in the ascending order of hardness which is determined in case of steels by carbon content and by heat treatment (hardened or nonhardened).

Table 2. The loads on various materials.

Fig. 6. Changes in the mean grain size o of a deformed zone versus the depth h of removed layer.

Fig. 7. The maximum visualization depth h_{max} of a deformed zone where the contrast disappears versus hardness H_B of steels under load $P = 1500$ kg.

Fig. 8. The maximum depth h_{max} where the deformed-zone contrast disappears versus applied load P for different materials.

Fig. 9. Picture of the trace of digit 2 obtained with successive polishing and ion etching for steel-20.

Fig.10. Variations of the width D of a deformed-zone trace with the depth h of removed layer.

Fig.11. The maximum depth h_{max} where the deformed-zone contrast disappears versus load P at different energies of incident ions.

Fig.12. Variations of the deformed-zone trace width with the removed layer depth at different energies of incident Ar^+ ions for Cu.

Fig.13. The same as in Fig. 12 for different loads.

Fig.14. Pattern of a deformed zone for Cu.

Table 3. The maximum depth at which a deformed zone is visualized in case of electrochemical and ion etchings.

Fig.15 (a, b, c). The shapes of samples and the locations where the load and the irradiation were applied.

Fig.16. Carbon distribution on a deformed steel surface irradiated by 40 keV Ar^+ ions.

Fig.17(a). Depth distributions of argon and carbon atoms in a copper cross-section irradiated by 40 keV Ar^+ ions.

Fig.17(b). Schematics of the cross-section used for depth distributions in Fig. 17(a): 1 - deformed region; 2 - undeformed area; 3 - probe guiding line in the X-ray microanalysis.

Fig.18. Carbon distribution in the deformation zone, cross-section of a copper sample was used.

Fig.19. Carbon distribution on the copper surface across the deformation zone. The sample was annealed for one hour at $T = 650^oC$.

Fig.20. Copper and tin distributions on bronze surface across the deformation zone after polishing the sample.

Fig.21. Auger electron spectra of a bronze surface before polishint (1) and following irradiation by 40 keV Ar^+ ions (2).

Fig.22. Copper and tin distributions on bronze surface across deformation zone after the irradiation by 40 keV Ar^+ ions.

Fig.23. The Ar^+ ion distribution in horseshoe-shaped samples.

Fig.24. The Ne, Ar, and Xe distributions.

1

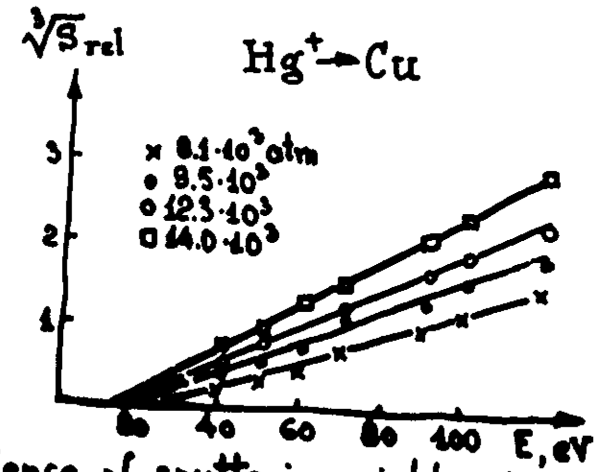

Dependence of sputtering yield on ion energy for different pressures
[Sh.G. Askerov and D.M. Nasrullaev, 1976]

2

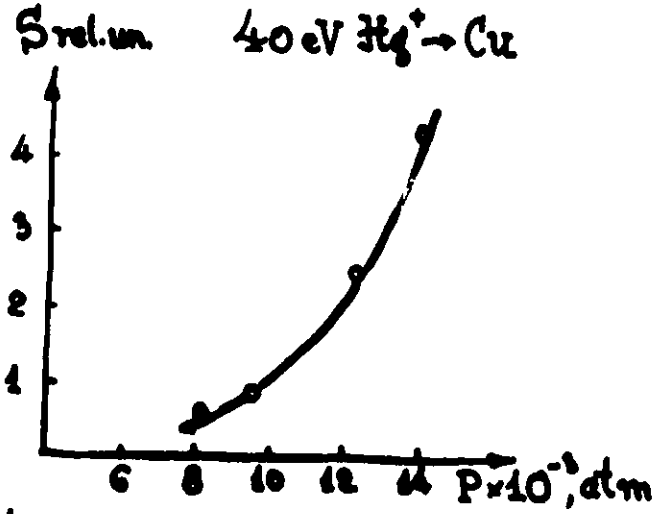

Dependence of sputtering yield on pressure
[,]

3

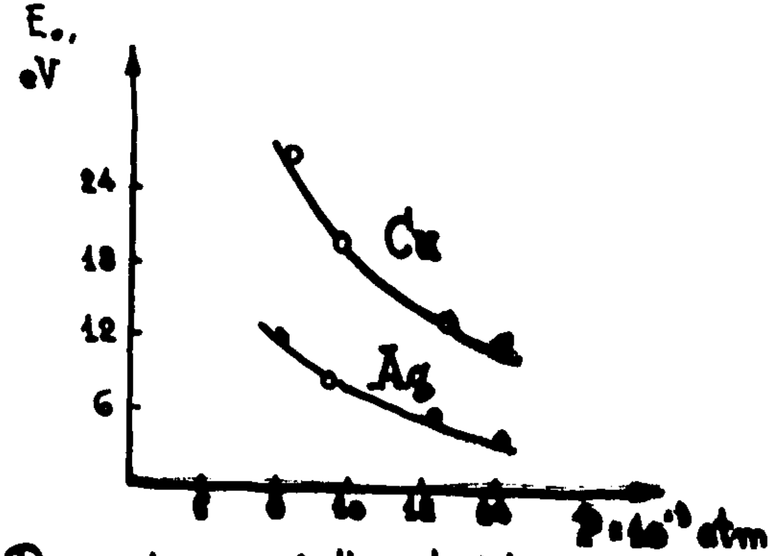

Dependence of threshold sputtering energy on pressure for Cu and Ag.

4

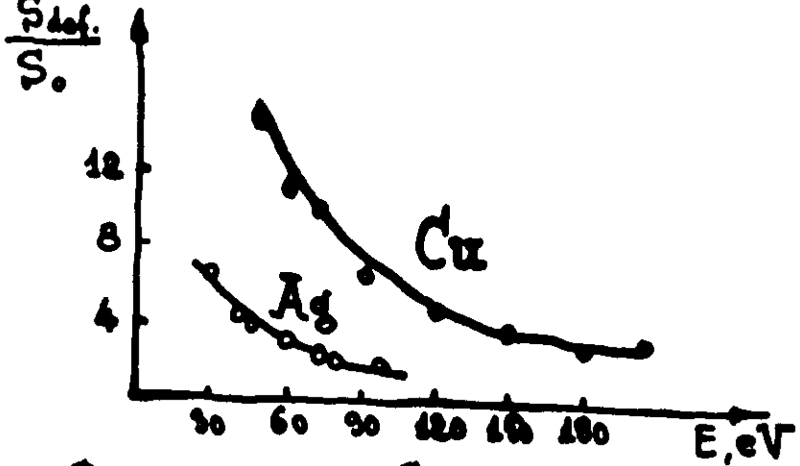

Dependence of $\frac{S_{def}}{S_0}$ on ion energy for $P = 9.5\cdot10^3$ atm.

5

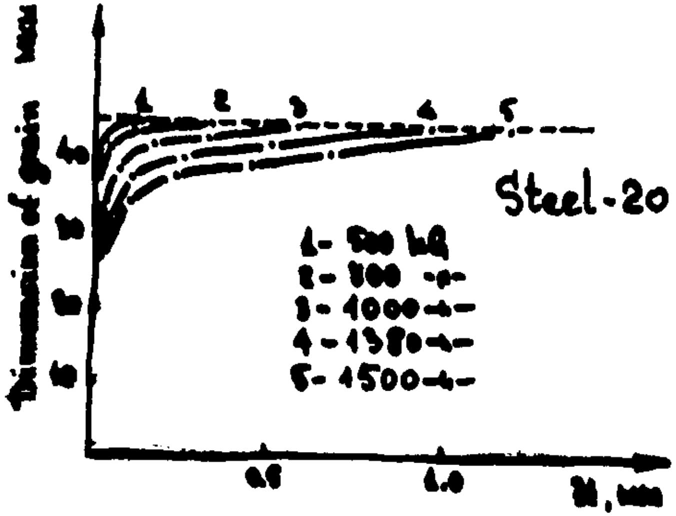

Variation of mean dimension of microstructure grain with depth.

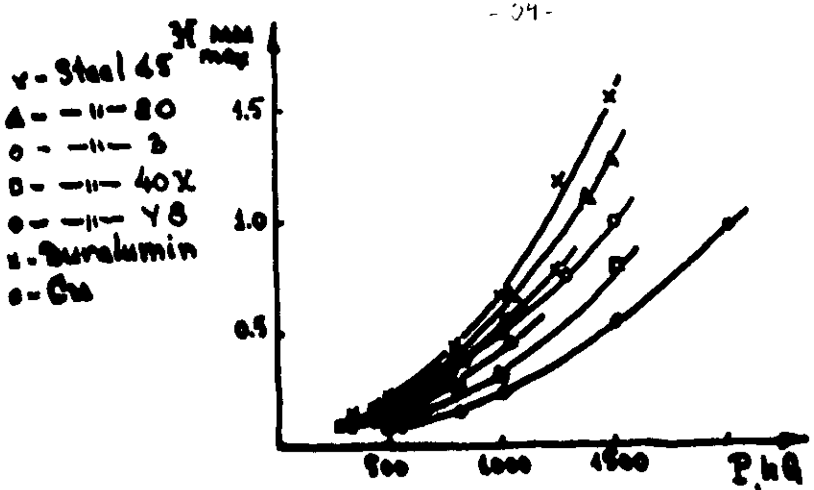

Dependence of visualized sign depth H_{max} on load P.

6

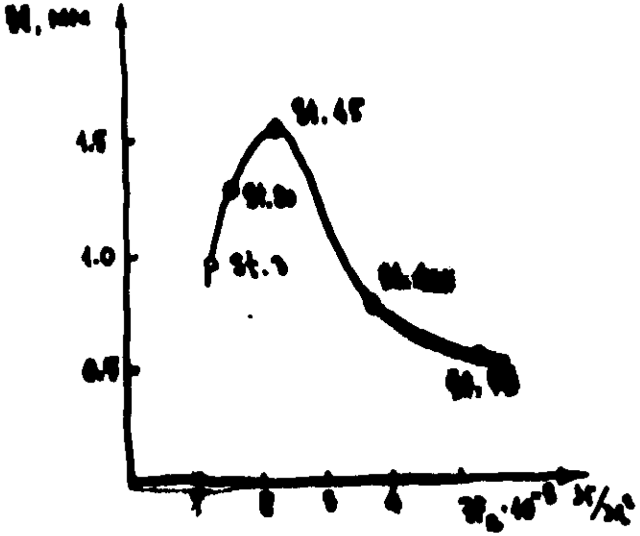

Dependence of visualized sign depth H on hardness of material H_B.

8

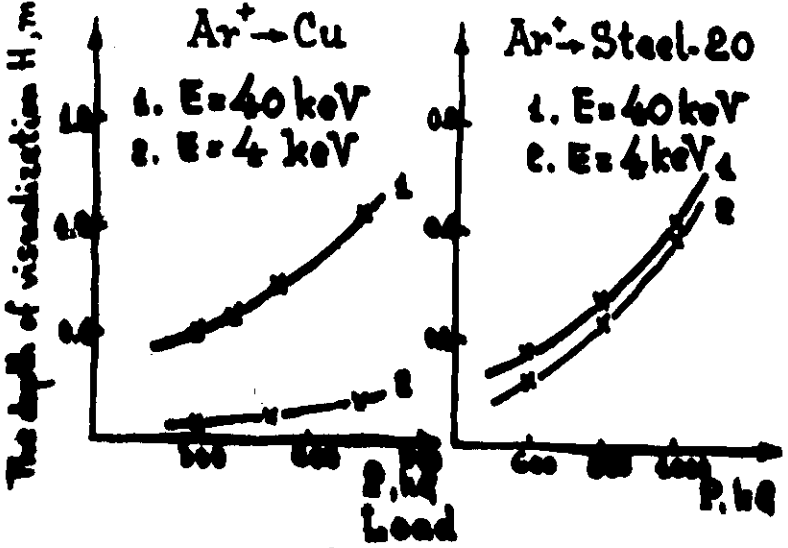

Dependence of the depth of visualization of sign H_{max} on load P.

9a

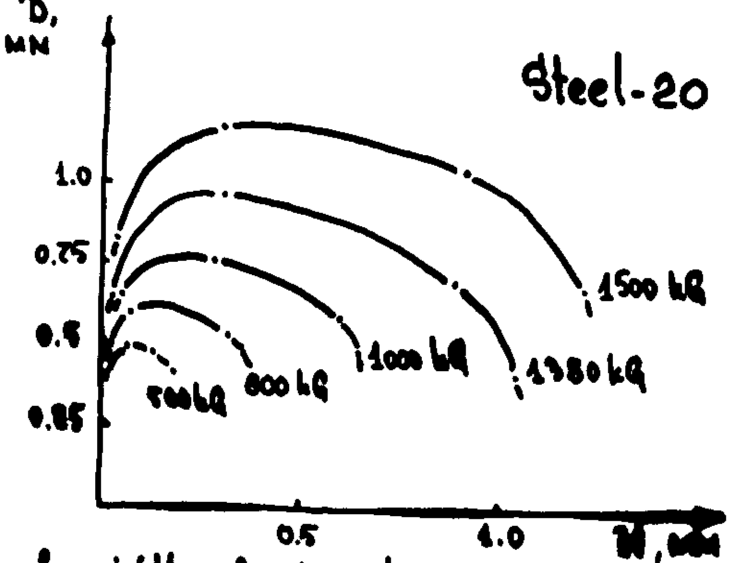

Variation of width of sign trace with depth for steel-20.

9b

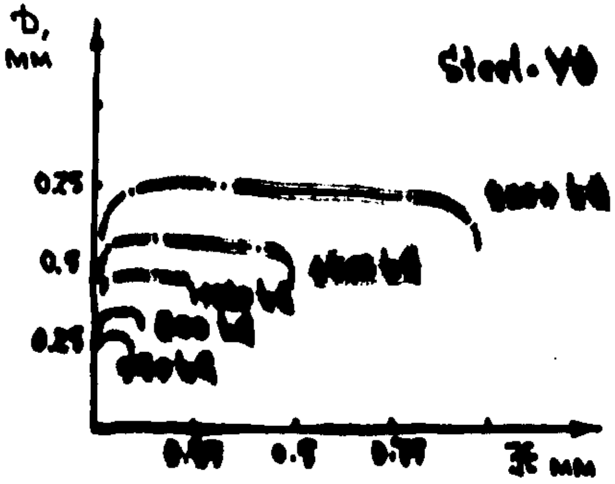

Variation of width of sign trace with depth for steel-Y8

9c

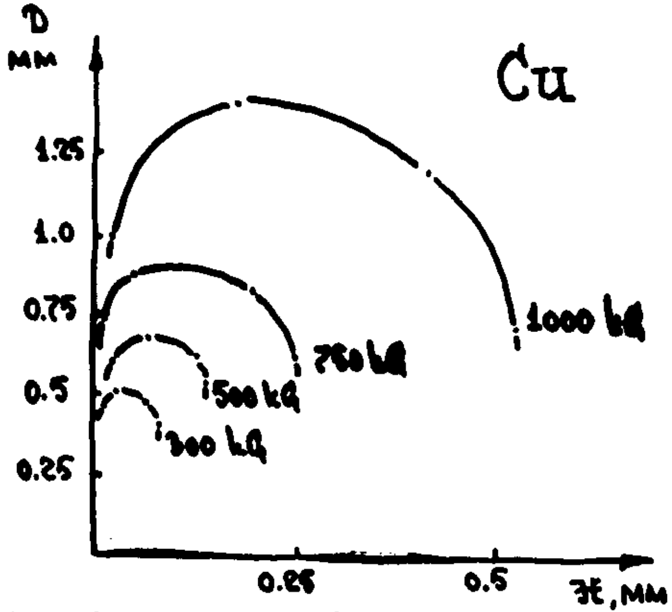

Variation of width of sign trace with depth for copper.

9d

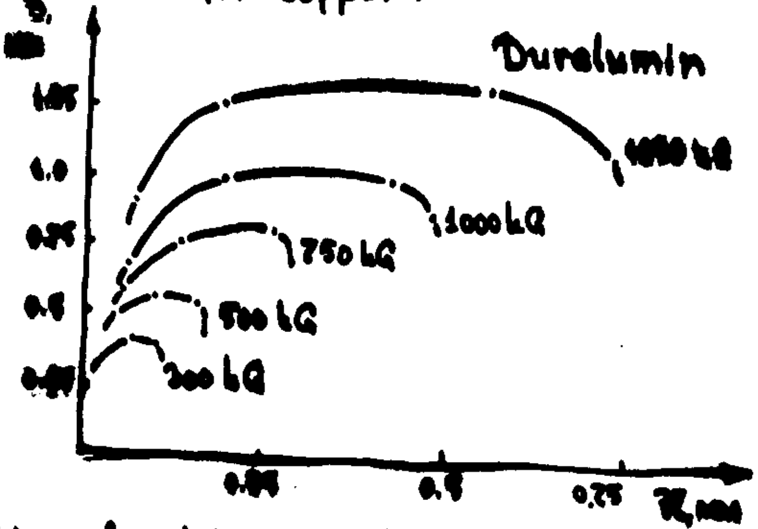

Variation of width of sign trace with depth for duralumin.

10.

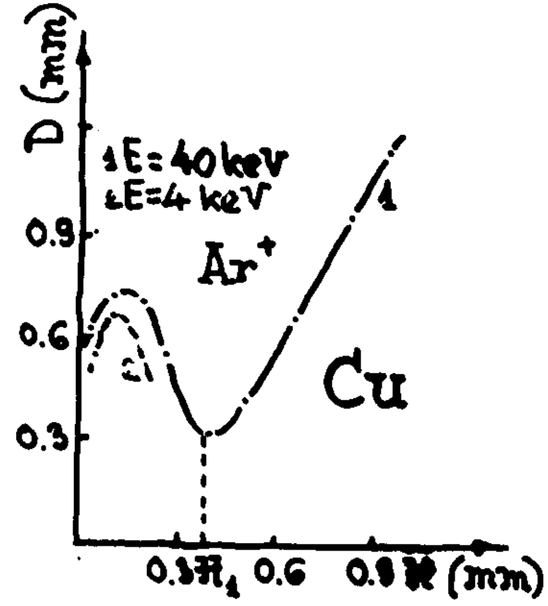

Dependence of the sign width on depth for Cu.

11.

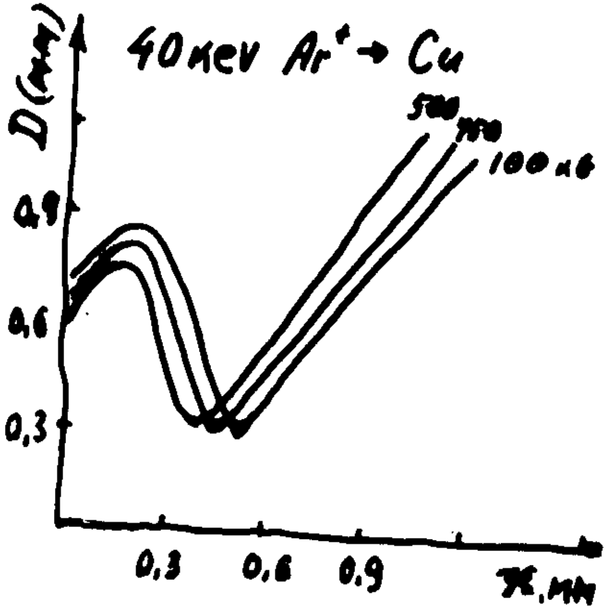

12

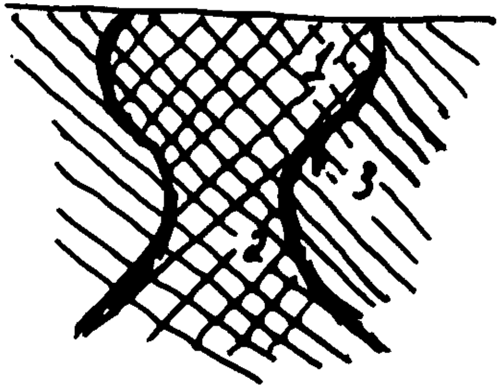

Scheme of deformed zones

Cross-section of target with different loads

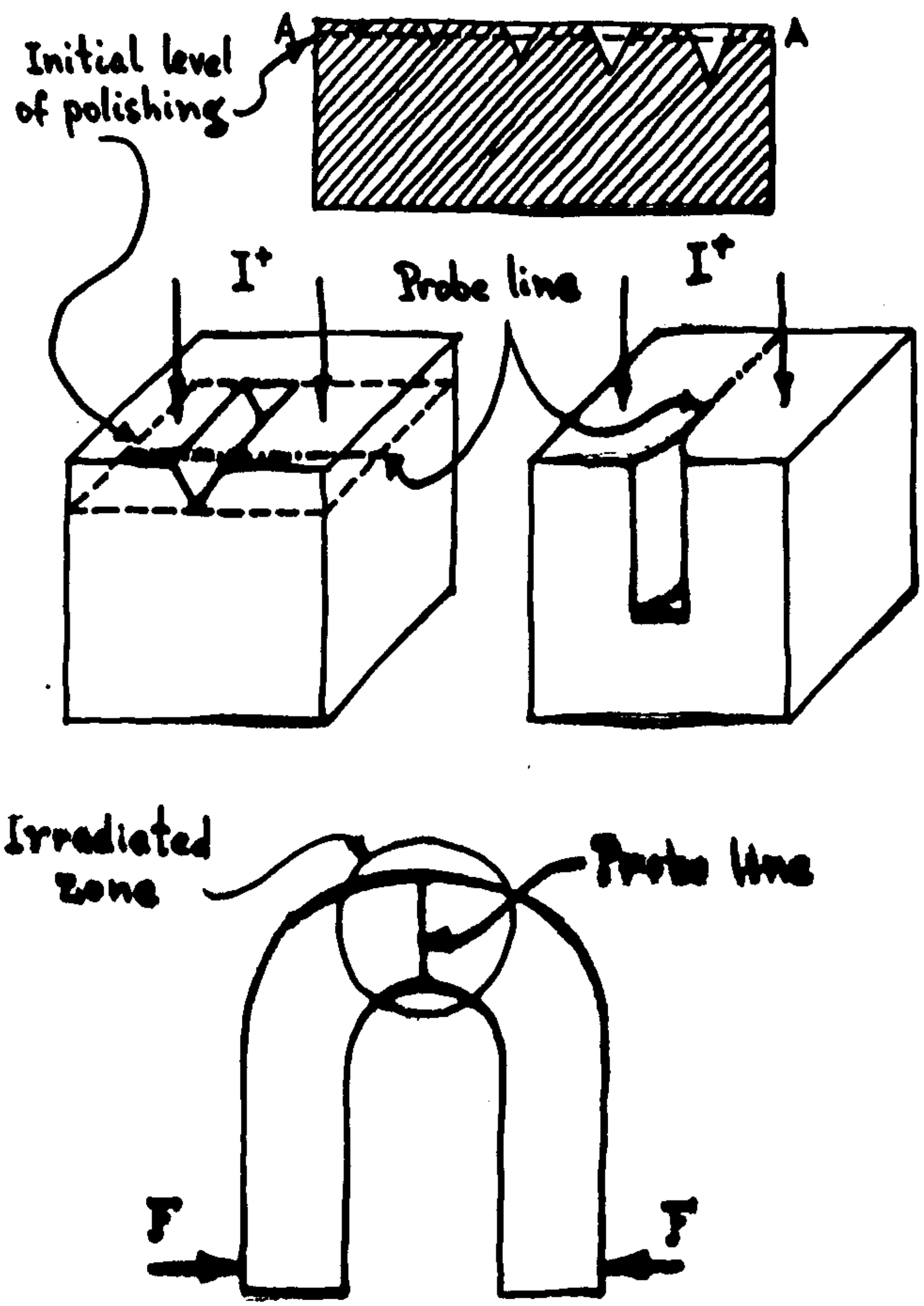

14.

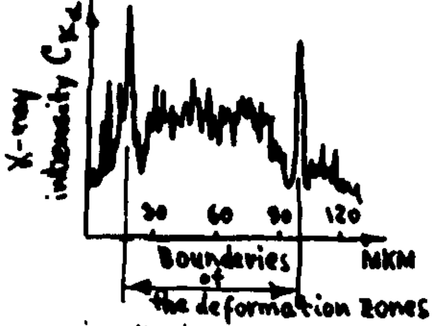

[illegible] distribution on a deformed [illegible] surface irradiated by 40 keV / Ar⁺ ions.

17.

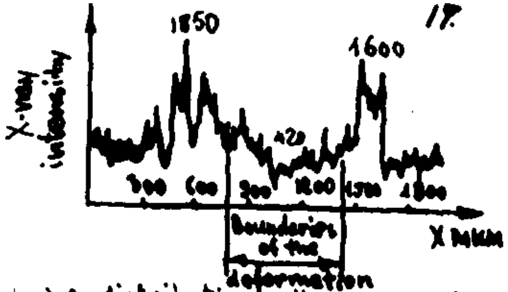

[illegible] distribution on the copper surface across the deformation zone. The sample was annealed for one hour at 650°C.

16.

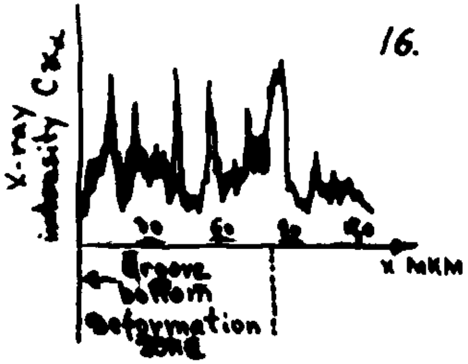

Carbon distribution in the deformation zone, cross-section of a copper sample was used.

15a.

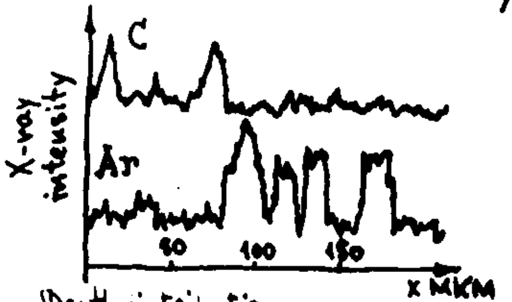

Depth distribution of argon and carbon atoms in a copper cross-section irradiated by 40 keV / Ar⁺ ions.

15.b

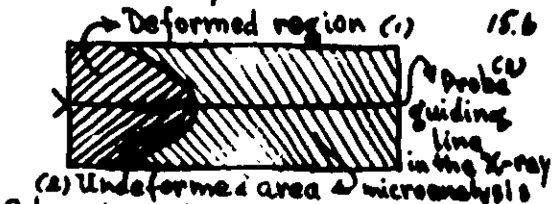

Schematics of the cross-section used for depth distributions.

20a.

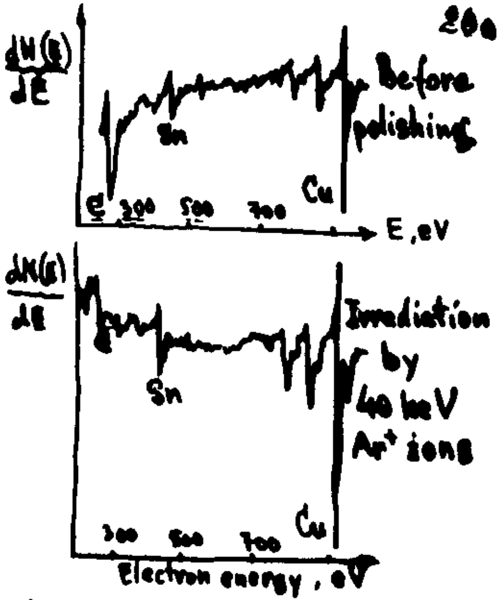

Auger electron spectra of a bronze surface.

18.

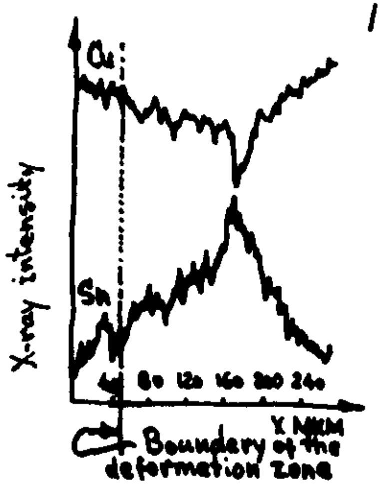

Copper and tin distributions on bronze surface across the deformation zone after polishing the sample.

20.

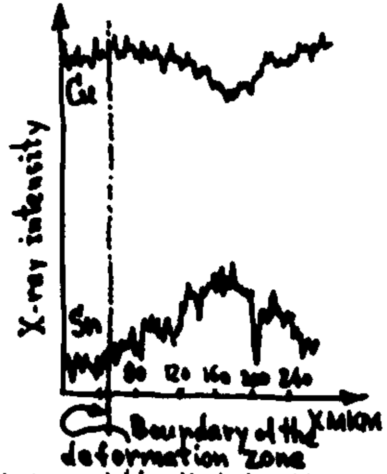

Copper and tin distributions on bronze surface across the deformation zone after the irradiation by 40 keV Ar⁺ ions.

19a

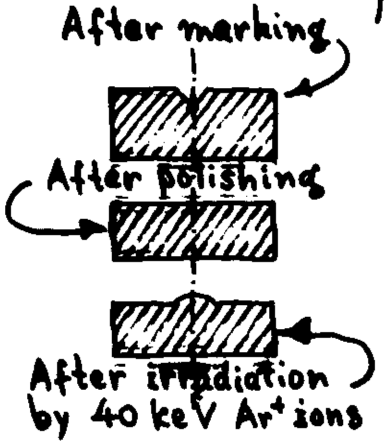

Schematic of the cross-section of the sample.

19

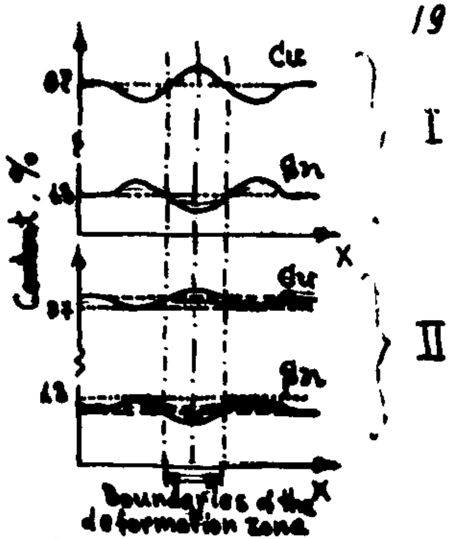

Schematics of the copper and tin distributions on a bronze surface after sample polishing (I) and following irradiation by 40 keV Ar⁺ ions (II)

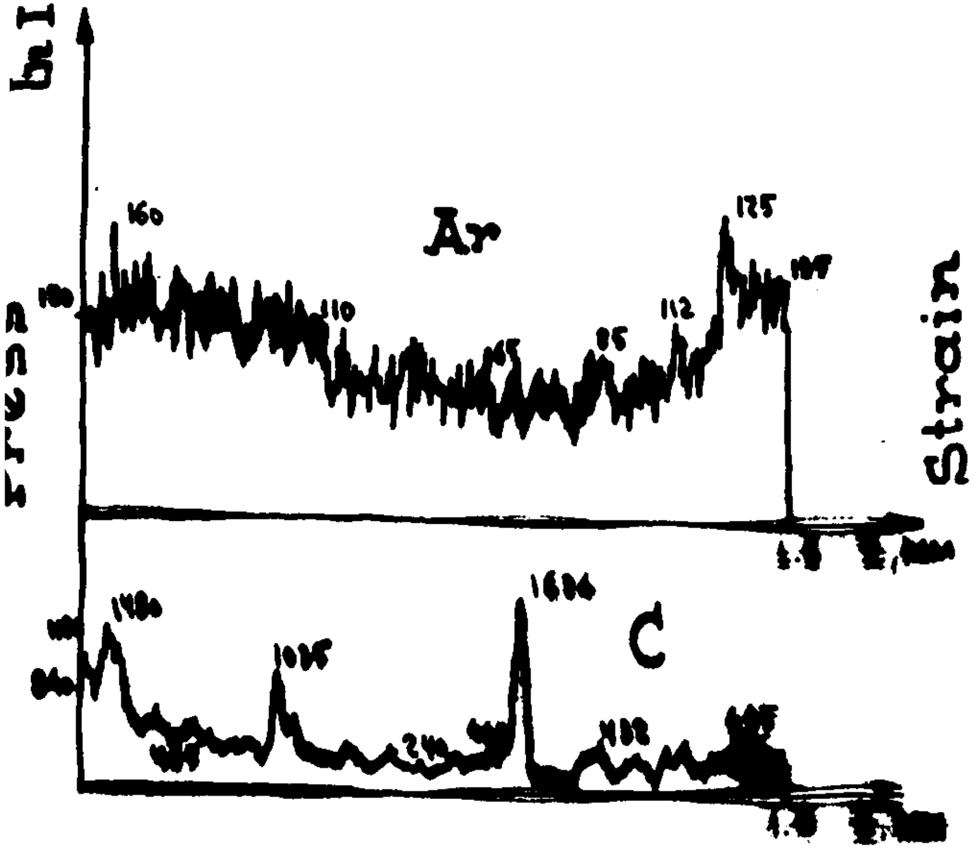

Micro X-ray analysis of "horseshoe" bronze sample along probe line.

Table 3.

Material	Load,	The discovered depth, [illegible] Electrodes: 4 keV; [illegible]		
Copper	500	0.17	0.21	[illegible]
Steel-20	1000	[illegible]	0.68	[illegible]

Table 1.

aterial	Hardness $(H_B)\cdot 10^{-7}\frac{N}{M^2}$	Content (%) of carbon	Temperature treatment
Cu	87	–	–
Duralumin	90	–	Tempered
Steel-3	131	0.14-0.22	–
–"– -20	163	0.17-0.24	–
–"– -45	229	0.42-0.49	–
–"– -40x	370	0.37-0.45	Tempered
–"– -Y8	550	0.69-0.73	–

Table 2.

Sample material	Load, kg				
	Number of sign				
	[illegible]	[illegible]	[illegible]	4	[illegible]
Cu	[illegible]	[illegible]	[illegible]	1000	*
Duralumin	[illegible]	[illegible]	[illegible]	1000	[illegible]
Steel-3	[illegible]	[illegible]	1000	1300	[illegible]
–"– -20	[illegible]	[illegible]	1000	1330	[illegible]
–"– -45	[illegible]	[illegible]	1050	1250	[illegible]
–"– -40x	[illegible]	[illegible]	1000	1500	–
–"– -Y8	[illegible]	[illegible]	1000	1500	[illegible]